



FINITE ELEMENT ANALYSIS OF INTERFACIAL CRACK PROPAGATION BASED ON LOCAL SHEAR, PART II—FRACTURE

HERZL CHAI

Department of Solid Mechanics, Materials and Structures, Tel-Aviv University, Tel-Aviv,
 Israel

and

MARTIN Y. M. CHIANG

Polymers Division, National Institute of Standards and Technology, Gaithersburg, MD 20899,
 U.S.A.

(Received 3 May 1996; in revised form 14 February 1997)

Abstract—The mechanics of fracture of a stably extending interface crack in polymeric adhesive bonds undergoing very large shear deformation is studied using a rate-dependent finite element analysis. Plane-strain and J_2 plasticity conditions are considered. Based on recent experimental observations, it is assumed that the local engineering shear strain at a certain distance (i.e. for the polymer adhesive studied, approximately a tenth bond thickness) straight ahead of the crack tip remains constant during the crack propagation. This critical strain is rate dependent, being a function of the crack velocity. The proposed fracture criterion is applied to several experimental crack growth histories pertaining to different specimen geometries, bond thicknesses and crack velocities. Although the analysis is highly sensitive to rate effects and other material characteristics, the comparison is generally reasonably successful. The analysis also provides quantitative insight into the mechanics of other failure modes observed in the experiments. In particular, the growth of a detrimental microdebond which is formed several bond thicknesses ahead of the crack tip seem to be controlled by the bond-normal tensile stress while hydrostatic tensile stresses appear responsible for the development of a kink or a large void at the crack tip which temporarily arrests the crack. All these and other failure modes are activated under large strains, which manifests the important rule of plasticity in the fracture of polymeric joints. © 1997 Published by Elsevier Science Ltd.

1. INTRODUCTION

Fracture tests on a toughened-epoxy adhesive bonds deforming in shear show that the fracture process is characterized by a stable crack propagation along one of the two interfaces of the bond which is followed by catastrophic growth [Chai (1993); Chai and Chiang (1996)]. A number of competing failure modes may be activated during the fracture process, the specific choice of which depends on the adhesive ductility, the initial crack position within the bond, the bond thickness and the loading level. In Part I of this work, the crack tip deformation field for the end-notched flexure (ENF) adhesive bond specimen and the rigid-substrates models (see Part I or Figs 1 and 10) is determined using a large-strain finite element analysis. The analysis shows that along the interface straight ahead of the crack tip, where the fracture mainly occurred, the distribution of the engineering shear strain, γ , conforms to the following singular form [eqn (4) of Part I]:

$$\gamma = K\bar{x}^{-\delta}, \bar{x} = x/h \quad (1)$$

where x is the horizontal axis originating from the crack tip (see inset in Fig. 1), h is the bond thickness and δ and K are dimensionless quantities obtained from the numerical analysis which magnitudes depend only on the average shear strain in the bond, $\bar{\gamma}$ (i.e. the relative shear displacement across the bond, Δ , divided by h). Equation (1) is found to apply well under small scale yielding conditions as well as beyond general yield (of the

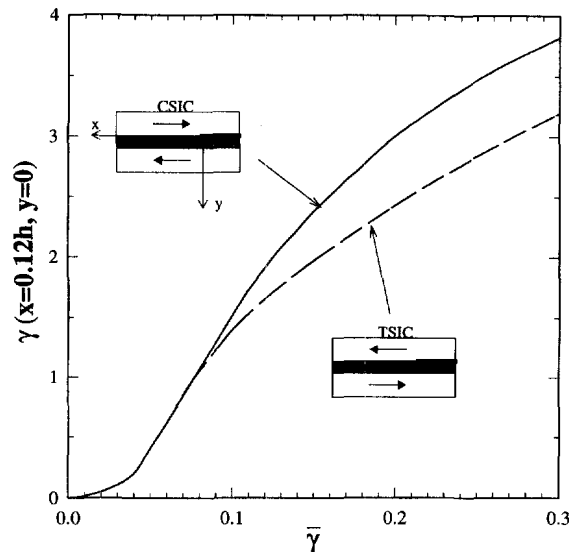


Fig. 1. The variation of the interface shear strain at $x = 0.12 h$ with the applied average shear strain; rigid substrate models, static analysis.

adhesive) for both the ENF and the rigid-substrates models. In this part of the work, the stable crack propagation phase is treated, with the main goals being to establish a valid interfacial crack propagation criterion and to illuminate the mechanics of the other failure modes observed.

Stable crack growth which precedes catastrophic fracture is a commonly observed phenomenon in testing ductile metals [e.g. Broek (1986)] or polymers [e.g. Williams (1984)]. The fracture work, often evaluated using the J integral technique, typically exhibits a “resistance” behavior. The fracture resistance curve is affected by the specimen geometry, however, and as such may not be a true material property. The case of fracture under large-scale yielding conditions is even more cumbersome. A commonly used fracture criterion in this case is the crack tip opening displacement (CTOD) due to Wells (1963). This concept, originally developed for monolithic materials, was later extended by Liechti and Knauss (1982) to adhesive bonds subjected to a combined tension and shear loadings. The practical implementation of this approach is somewhat ambiguous, however, because at the crack tip the CTOD vanishes. Moreover, this quantity may also depend on the specimen geometry. Crack tip opening angle (CTOA) is another popular crack propagation criterion. However, as discussed by Rousselier (1979), the CTOA may depend on the specimen geometry, and, for a given specimen, its value at the onset of crack propagation may differ from that during the stable growth. Further difficulties in assessing fracture may arise when the material is tested as a thin bond because, in addition to exhibiting a “resistance” behavior, the shearing fracture work in this case also depends on the interlayer thickness [Chai (1988, 1993)]. The present study attempts to identify a fracture criterion based on local strains (rather than displacements or strain energy) which is independent of the specimen geometry and which, apart from being rate sensitive, remains constant during the crack propagation event.

The fracture problem at hand encompasses some complex phenomena including very large deformations, friction between the debonded interfaces, elastic unloading and material rate effects. Considering the wide range of assumptions naturally involved in such analysis, and with the view toward quantitative correlation with the results of the fracture tests reported in Chai and Chiang (1996), all material parameters used in the finite element analysis, including the adhesive stress–strain behavior, the friction law for the debonded interfaces and the adhesive rate dependence, are experimentally determined.

2. NUMERICAL ANALYSIS

The Abaqus finite element program (1994), particularized to plane-strain, large deformation and incremental plasticity, is employed. The adhesive analyzed is nearly elastic

perfectly-plastic (Part I), with a yield strain in shear, γ_Y , equals 0.06. J_2 plasticity with isotropic strain hardening is assumed for the adhesive while the adherends are either linearly elastic or rigid. General details of the analysis, including the dependence of the adhesive yield stress on the strain rate and the effect of friction between the debonded interfaces, are reported in Part I. Numerical results are presented for the ENF specimen and the rigid-substrates models. In both cases, the CSIC (compression side interface crack) and the TSIC (tension side interface crack) bond configurations are analyzed. As shown in Part I, the rigid-substrate models accurately describe the crack tip behavior for the more complex ENF and Butterfly test specimens used in the previously mentioned experiments. As will be seen later, however, the rigid-substrates models are inadequate when dealing with damage events (e.g. microdebonding) which are controlled by the stress state well ahead of the crack tip. In such cases, the full-fledged ENF specimen is analyzed.

3. CRACK PROPAGATION CRITERION

The conditions for interfacial cracking is inferred from the distribution of the engineering shear strain straight ahead of the crack tip. As shown in Fig. 10 of Part I, eqn (1) compares well with the experimental shear strain except over approximately a tenth bond thickness long zone immediately ahead of the crack tip, where the analytical shear strain seem to increase without bounds towards the crack tip while the experimental one remains essentially constant. The accuracy of the numerical data in that critical zone is assessed (Part I) by employing various degrees of mesh refinement. With the finest mesh used, the solution converges only up to approximately a tenth bond thickness from the crack tip. It is quite possible that the singular behavior given by eqn (1) is, in fact, inapplicable in regions yet closer to the crack tip. Moreover, a breakdown of constitutive assumptions in that highly stressed zone may also affect the behavior there. To circumvent the cumbersome issue of strain singularity, it is assumed in this work that fracture initiates when the local shear strain at a certain distance straight ahead of (rather than at) the crack tip, x_0 , reaches a critical value.† Fortunately, the fracture tests provide the necessary information to unambiguously determine x_0 .

As shown in Chai and Chiang (1996), for the particular toughened epoxy adhesive tested, the onset of crack propagation for both the ENF and the Butterfly joints occurred when the local shear strain at the crack tip, γ_t , reached the critical value

$$\gamma_t^c = 1.6\text{--}1.8. \quad (2)$$

Although this value is associated here with the crack tip, the exact location of which it was measured is obviously affected by the resolution of the detecting apparatus. However, this does not appear to be of a great concern in work since the test results suggest that the shear strain changes only little in the immediate vicinity of crack tip (e.g. Fig. 10 of Part I). The relationship in eqn (2) was also found equally well for both the CSIC and TSIC bond configurations over the entire bond thickness studied (i.e. 25–420 μm). This value was maintained irrespective of whether the fracture occurred from a precrack or from a kink formed sometime during the growth. In the latter case, the background or average shear strain in the bond at the onset of crack propagation could be nearly as large as the local shear strain given by eqn (2). For a crack propagating from an insert under continuously increasing load, the fracture for both the ENF and the Butterfly specimens occurred when the average shear strain at the crack tip region, $\bar{\gamma}_t$, reached the specific value:

$$\bar{\gamma}_t = 0.10\text{--}0.12. \quad (3)$$

It should be noted that this value, found to apply to all bond thicknesses attempted, i.e. in the range 70–280 μm , may depend on the specimen geometry, and as such it cannot serve

† A somewhat similar proposition was made by McClintock (1958), who, in his static analysis of Mode III cracks in metals, hypothesized that "fracture initiates when a critical shear strain is attained throughout a critical volume of material" ahead of the crack tip. No conclusive experimental substantiation of this was given, however.

as an alternative criterion for predicting the onset of crack propagation. Since, in the case of the rigid-substrates models, on the basis of a bond thickness normalized length scales (i.e. x/h , y/h) the elastoplastic fields for a given average shear strain are independent of h and, since γ_i^c is also independent of h , one concludes that x_0 can be normalized with respect to the bond thickness. Under these conditions, to determine \bar{x}_0 for the present test specimens one needs only to substitute eqns (2) and (3) in eqn (1):

$$\bar{x}_0 = [K(\bar{\gamma} = 0.11)/1.7]^{1/\delta(\bar{\gamma}=0.11)} \quad (4)$$

where $\bar{x}_0 = x_0/h$. The problem is further simplified by observing from Figs 7 and 8 of Part I that the values of $K(\bar{\gamma} = 0.11)$ and $\delta(\bar{\gamma} = 0.11)$ are nearly the same for both the CSIC and the TSIC configurations, being equal to 0.39 and 0.70, respectively. Substituting this in eqn (4), one finds for the present ENF and rigid-substrates models:

$$\bar{x}_0 = 0.12. \quad (5)$$

The dependence of the interface shear strain at $\bar{x} = \bar{x}_0$ on $\bar{\gamma}$ is then found by substituting eqn (5) in eqn (1):

$$\gamma(\bar{x}_0) = 0.12^{-\delta(\bar{\gamma})} K(\bar{\gamma}). \quad (6)$$

Figure 1 shows the variation of $\gamma(\bar{x}_0 = 0.12)$ with load as determined from eqn (6) using the numerically obtained relationships between δ and $\bar{\gamma}$ and K and $\bar{\gamma}$ given in Part I. The local shear strain for the CSIC and the TSIC configurations seem nearly identical up to the onset of crack propagation ($\bar{\gamma} = 0.11$). Thereafter, the two configurations significantly diverge. However, the stationary crack analysis in that loading range no longer applies.

It is assumed here that the characteristic length given by eqn (5) applied not only to the onset of crack propagation, but also to the entire interfacial crack growth that follows. The motivation for this choice is discussed later in this work. Under this assumption, the entire crack propagation event must conform to the following constraint:

$$\gamma(\bar{x}_0) = \gamma_i^c. \quad (7)$$

The fracture tests pertaining to the adhesive under consideration showed that γ_i^c exponentially decays with the crack velocity, v , in accordance with the following curve-fitting relationship [Chai and Chiang (1996)].

$$\gamma_i^c(v) = 1.7 - 0.8(1 - e^{-0.23v}), \quad (8)$$

where the units of v are in $\mu\text{m s}^{-1}$. Using eqn (8) in eqn (7), the fracture criterion for the present adhesive takes the form

$$\gamma(\bar{x}_0) = 1.7 - 0.8(1 - e^{-0.23v}). \quad (9)$$

Thus, for example, for a crack propagating at a constant velocity of $5 \mu\text{m s}^{-1}$, the shear strain at $x = 0.12 h$ should be maintained at 1.15 throughout the growth.

4. RESULTS AND DISCUSSION

A brief review of some relevant results from the fracture tests mentioned earlier is in order. As demonstrated in Fig. 2, four different failure modes may occur during the fracture process, namely interfacial cracking, crack kinking, voiding at the crack tip and development of a microdebond at the interface ahead of the main crack. The conditions governing these failures are summarized in Fig. 3. A crack initially residing on the compression side interface maintains its position up to catastrophic failure regardless of the bond thickness. The latter phenomenon is triggered by the emergence of an interface microdebond approximately 4–8 bond thicknesses ahead of the tip of the main crack, see Fig. 2(a). The load necessary to initiate the microdebond, $\bar{\gamma}_i^d$, monotonically increases with

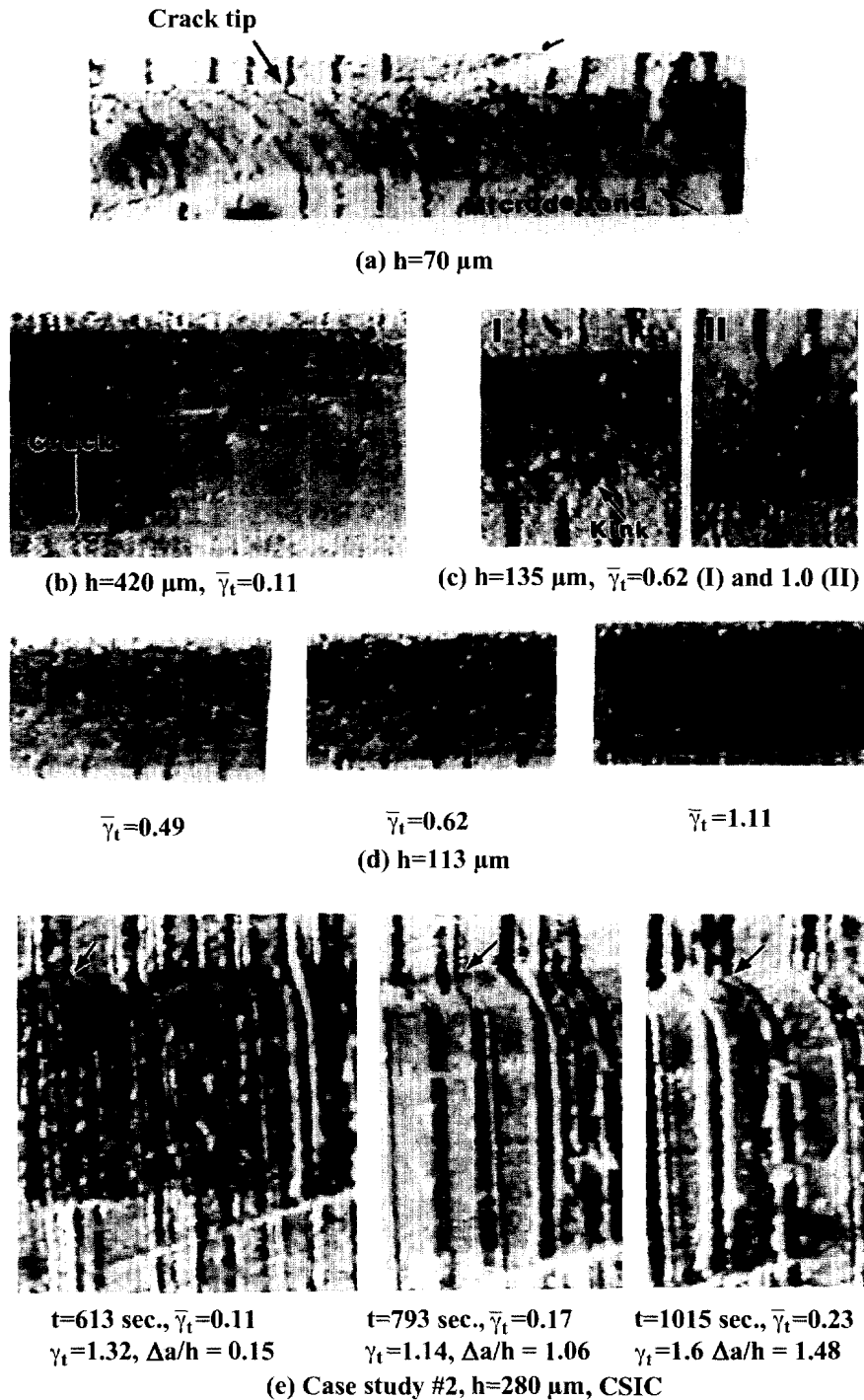


Fig. 2. Video micrographs from ENF tests [Chai and Chiang (1996)] showing the various failure modes which may occur during the fracture process for a toughened epoxy adhesive (BP-907, American Cyanamide). (a) interfacial cracking (upper interface) and microdebonding ahead of the main crack (lower interface); (b) and (c) crack kinking in a relatively thick and a relatively thin bond, respectively; (d) void growth; (e) the crack tip region at three instants during crack propagation, case study no. 2. The arrows in (e) indicate the crack tip position. Note that the first print on the left has a lower magnification than the other two prints.

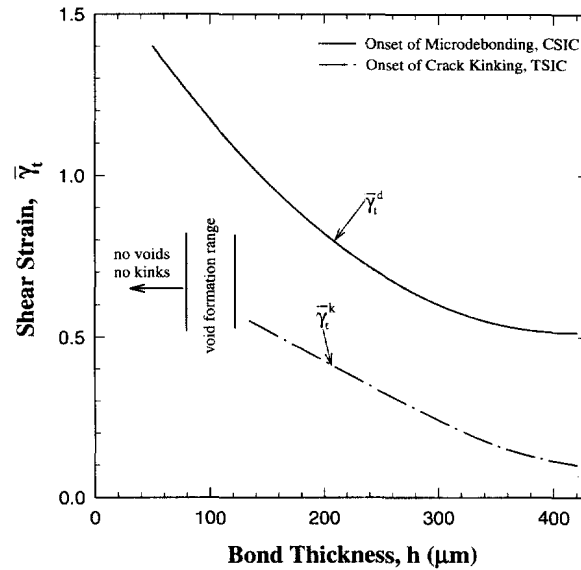


Fig. 3. Summary of the dependence of the activation conditions for the various failure modes observed in the ENF tests of Chai and Chiang (1996).

decreasing h . The growth history for a tension side interface precrack is more involved. For $h > 130 \mu\text{m}$, the crack always kinks from the tension to the compression side interface sometime during the growth. The load at which this occurs, $\bar{\gamma}_t^k$, decreases with increasing h . In fact, for the thickest bond tested ($420 \mu\text{m}$), crack kinking just preceded the onset of interfacial cracking. Once on the compression side interface, the crack continues to grow as for the CSIC case. For $h < 70 \mu\text{m}$, no kinking occurs while in the intermediate range, $70 \mu\text{m} < h < 130 \mu\text{m}$, a large void develops at the crack tip which precludes further crack growth. Each of these failure modes is discussed in the following.

4.1. Interfacial crack propagation

The interfacial crack propagation analysis is carried out by using a node release scheme in the finite element program. Three experimental crack growth histories obtained in Chai and Chiang (1996) are analyzed. These case studies encompass different specimen geometries, bond thicknesses and precrack positions. The crack tip data measured during the fracture process are $\bar{\gamma}_t$, γ_t and Δa , where Δa is the crack extension. Figure 2(e) shows three videographs of the crack tip region for case study number 2. Indicated in these prints is the time, t , the instantaneous location of the crack tip and the measured average and local shear strains at the crack tip. The latter two quantities were determined based on the deformation of the initially vertical scratch lines shown in the prints. The variations of $\bar{\gamma}_t$ and Δa with time for the three case studies are depicted in Figs 4(a)–6(a) (filled squares and hollow triangles, respectively). It is advantageous to use the crack tip “loading” parameter, $\bar{\gamma}_t$, rather than time, as the main experimental variable. The corresponding variations of γ_t and the crack extension with $\bar{\gamma}_t$ are shown in Figs 4(b)–6(b) (filled circles and hollow triangles, respectively). Note that the variation of γ_t with load ($\bar{\gamma}_t$) are related to the changing crack speed incurred in these tests in accordance with the relationship given in eqn (8). The data for case study number 2 are limited to $\bar{\gamma}_t < 0.235$ because this test was erroneously interrupted before complete failure. Also, the data for case study number 3 are terminated at $\bar{\gamma}_t = 0.29$ since, starting from about this loading, a large void has developed at the crack tip which precluded further crack propagation [see Fig. 2(d)]. The treatment of such damage is beyond the scope of this work.

All three afore-mentioned case studies are modeled by the rigid-substrates configuration. (Note that in these cases the subscript “t” in $\bar{\gamma}_t$ is redundant). Since it proved difficult to directly enforce the constraint given by eqn (9), the proposed fracture criterion is assessed by inputting to the finite element program the experimental loading and crack extension histories, $\bar{\gamma}_t$ vs t and Δa vs t , and comparing the analytical prediction for $\gamma_t(\bar{x}_0)$ with the

experimentally obtain history of γ_t^c . The inputted experimental histories are represented by the solid lines in Figs 4(a)–6(a), which are composed of discrete linear segments. Figure 7 shows the deformed mesh for a given instant during the crack propagation (case study number 1). The local shear strain along the interface is established from the slope of the originally vertical grid lines belonging to the first row of elements below the upper interface.

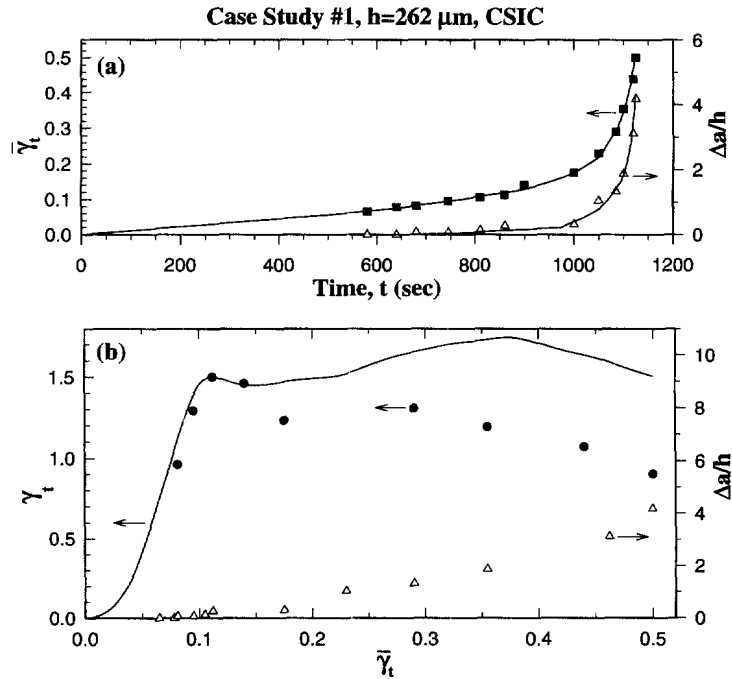


Fig. 4(a, b)

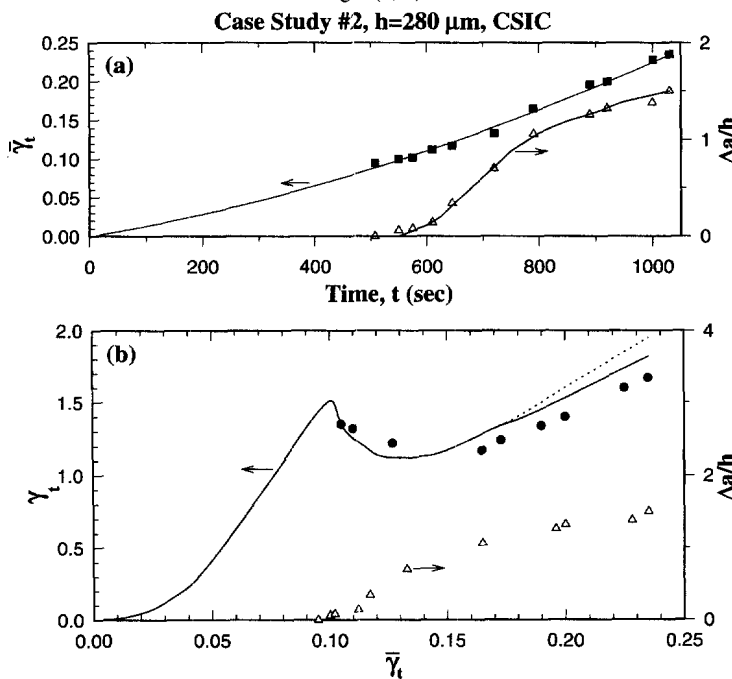


Fig. 5(a, b)

Figs 4–6(a). The variations with time of the average shear strain at the crack tip, $\bar{\gamma}_t$, and the crack extension, Δa , for three experimental case studies [Chai and Chiang (1996)]. The solid lines through the data represent the assumed input conditions to the finite element analysis; (b) corresponding variations with $\bar{\gamma}_t$ of the interface shear strain at the crack tip, γ_t , and the crack extension. The solid lines are the finite element predictions for γ_t at $x = 0.12 h$, $y = 0$. The dashed line in Fig. 5(b) corresponds to the finite element prediction for a zero friction between the debonded interfaces.

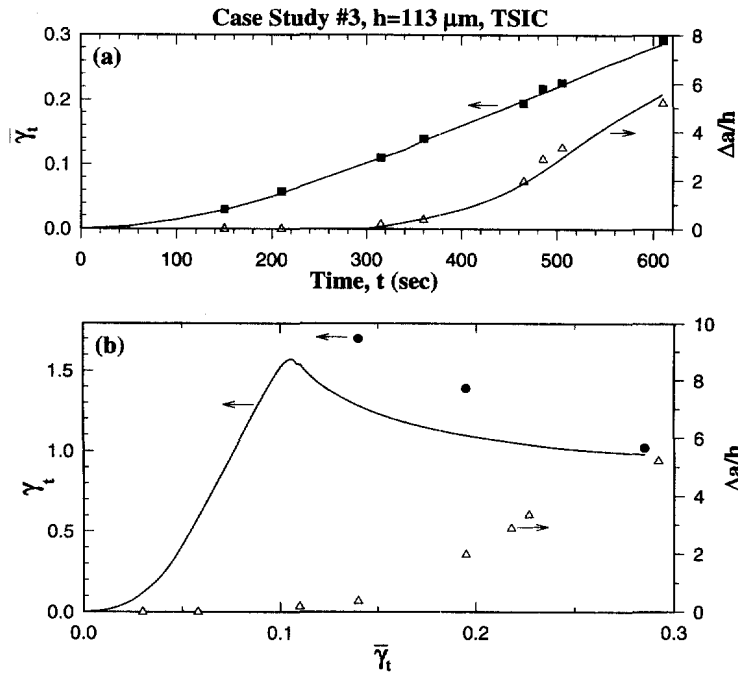


Fig. 6(a, b)

The distribution of shear strain, thus obtained, is given by the filled circles and the corresponding best-fit solid line in Fig. 7. Compared with the static analysis [eqn (1)], the decline of γ_t from the crack tip is very mild. For example, a variation of 25% about $\bar{x} = 0.12$ leads to only a small percentage change in the value of γ_t . It is for such a reasoning that we assume \bar{x}_0 to remain constant throughout the fracture event.

Figures 4(b)–6(b) (solid curves) shows the finite element predictions for the variations of γ_t ($\bar{x} = 0.12$). With $\bar{\gamma}_t$ for the three case studies under discussion. Comparison with the static analysis (Fig. 1) shows that the motion of the crack greatly reduces the otherwise monotonically increasing local shear strain at the crack tip. This knockdown manifests the important rule of material rate dependence on the fracture of polymers. The predicted local shear strains generally resemble reasonably well the experiments except for Fig. 4(b), where a rather large difference (up to 50%) between theory and experiment is developed once $\bar{\gamma}_t$

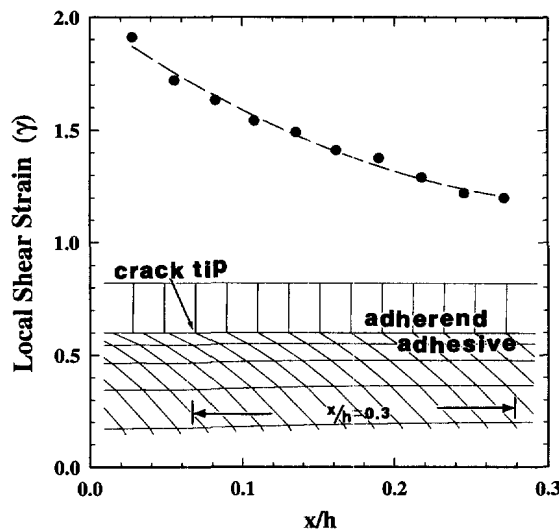


Fig. 7. Deformed finite element grid and corresponding variation of the local shear strain straight ahead of the crack tip (filled circles) for a given instant during the crack propagation for case study no. 2 ($\bar{\gamma}_t = 0.2$). The dashed line is a best fit to the data.

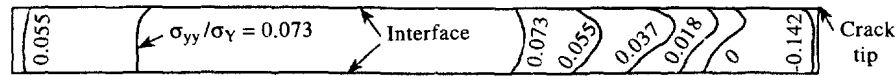
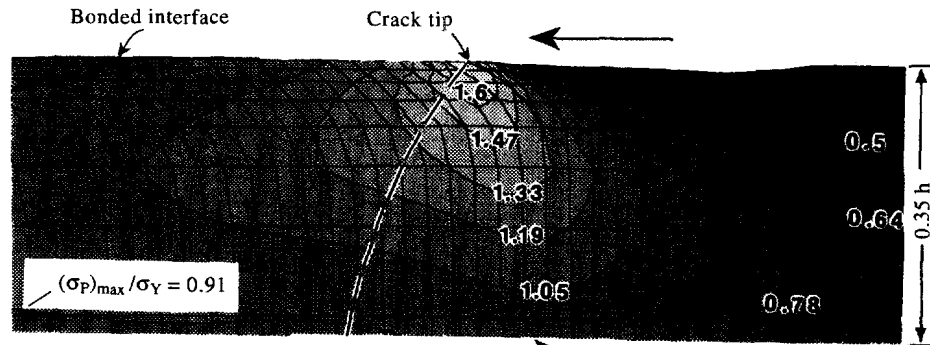
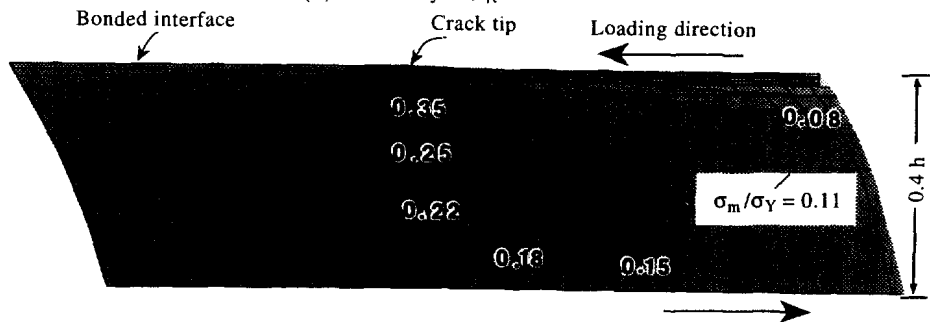
(a) ENF-CSIC, $h = 280 \mu\text{m}$, $\bar{\gamma}_t = 0.22$ (b) Case study #3, $\bar{\gamma}_t = 0.12$ (c) Case study #3, $\bar{\gamma}_t = 0.285$

Fig. 8. Contour plots at given instants during crack propagation: (a) σ_{yy} ; (b) maximum principal stress, $(\sigma_p)_{max}$. The dashed line indicates the path for which σ_p is maximized; (c) mean stress, $\sigma_m (= (\sigma_1 + \sigma_2 + \sigma_3)/3)$.

exceeds 0.3. Given the breadth of the problem, it is perhaps unrealistic to expect a much better correlation with the test results at our present knowledge of material flow behavior under very large strains and the level of precision of our experimental data. As indicated in the experimental work, the error in measuring γ_t , $\bar{\gamma}_t$ and Δa could be as large as 10%. Such scatter is found to lead to variations in the computed analytical variables which are of the same order of magnitude as the afore-mentioned differences. Another possible contribution for the departure between theory and experiments is the great sensitivity of the analysis to the material rate parameters (D and d , Part I) used. The latter are determined under small strain conditions, whereas the analysis deals with very large deformations. The neglect of the effect of pressure on the yielding behavior of the adhesive is another possible source of errors.

4.2. Microdebonding ahead of the main crack

The prospect that the microdebond ahead of the main crack is initiated by the bond-normal stress, σ_{yy} , is now examined. Because the stress distribution well ahead of the crack tip is of interest here, the ENF-CSIC specimen is analyzed. The input parameters in this case are the crack extension and the displacement, U , under the mid-span load, P . In consistency with the experiments, U is taken to increase linearly with time, at a constant rate of $2.2 \mu\text{m s}^{-1}$, while the crack propagation starts when $\bar{\gamma}_t$, calculated from the deformation of the finite element grid, reaches 0.11. Also the crack velocity is taken as $2 \mu\text{m s}^{-1}$. Figure 8(a) shows contours of constant σ_{yy} within the bond area around the crack tip at a given

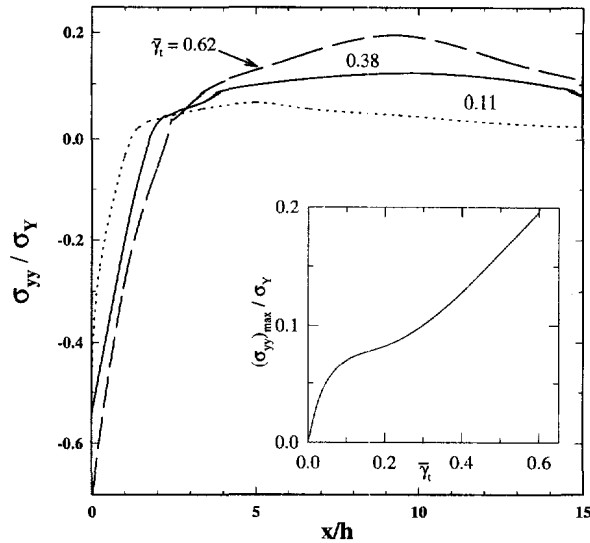


Fig. 9. Finite element prediction of the variation of the bond-normal stress along the bond center at three instants during the loading history; ENF-CSIC run, $h = 280 \mu\text{m}$, $v = 2 \mu\text{m s}^{-1}$, mid-span displacement rate equals $2.2 \mu\text{m s}^{-1}$. Note that crack propagation starts at $\bar{\gamma}_t = 0.11$. The inset shows the variation with $\bar{\gamma}_t$ of the maximum value of the tensile stress in the bond.

instant during the crack propagation ($\bar{\gamma}_t = 0.22$), while Fig. 9 details the variation of σ_{yy} along the bondline, starting from the crack tip, for several instants during the crack propagation event. The results, pertaining to $h = 280 \mu\text{m}$, conclusively show that σ_{yy} changes from compression to tension as the distance from the crack tip is increased, reaching its largest tensile value, $(\sigma_{yy})_{\text{max}}$, at a certain distance ahead of the crack tip which depends on $\bar{\gamma}_t$. Figure 9 (inset) shows that $(\sigma_{yy})_{\text{max}}$ monotonically increases with $\bar{\gamma}_t$, being approximately 20% of the yield stress at the onset of microdebonding for this particular test (i.e. $\gamma_t^d = 0.62$, see Fig. 3). At this instance, $(\sigma_{yy})_{\text{max}}$ is located approximately nine bond thicknesses ahead of the crack tip.

Since $\bar{\gamma}_t^d$ heavily depends on h (Fig. 3), similar ENF runs were conducted for other bond thicknesses (i.e. 60, 125 and 420 μm) to determine how this may affect $(\sigma_{yy})_{\text{max}}$. For each bond thickness, $(\sigma_{yy})_{\text{max}}$ was evaluated at that value of $\bar{\gamma}_t$ for which the microdebond ensued (Fig. 3). The results, displayed in Fig. 10 along with the corresponding values of $\bar{\gamma}_t^d$, show that $(\sigma_{yy})_{\text{max}}$ at the onset of microdebonding is essentially independent of the bond thickness, being approximately 20% of the adhesive yield stress. This, together with the

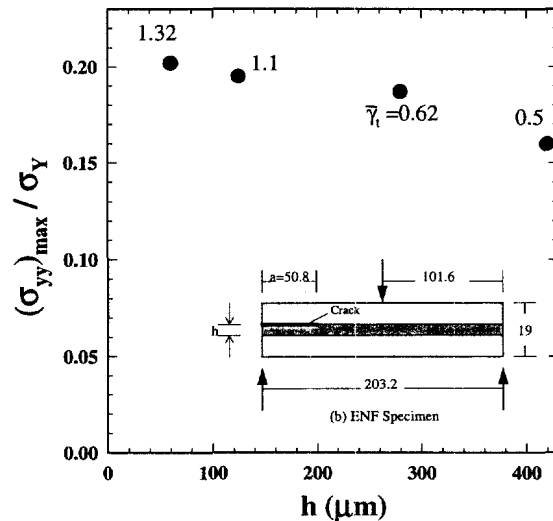


Fig. 10. Normalized $(\sigma_{yy})_{\text{max}}$ for several bond thicknesses-ENF runs. In each case, the value of $\bar{\gamma}_t$ in which $(\sigma_{yy})_{\text{max}}$ is evaluated corresponds to the value needed to initiate microdebonding. Inset dimensions are in mm.

fact that the locus of $(\sigma_{yy})_{\max}$ (8–9 bond thicknesses ahead of the crack tip in all cases) agrees well with the actual site of the microdebonds, strongly suggest that the bond–normal tensile stress is the main cause for the microdebond nucleation. It should be noted that this tensile stress acts in conjunction with the background shear stress in the bond. In all cases, the magnitude of this stress nearly coincides with the yield stress in shear. Once formed, the microdebond rapidly spreads along the interface in both directions, apparently under the same mechanism that drives the main crack, which leads to catastrophic failure. It should be noted at this point that for a given $\bar{\gamma}_t$, the distribution of the stress ahead of the crack tip would be affected by the specimen geometry (ENF, Butterfly, Lap joint, etc.). This implies that the onset of catastrophic failure also depends on the specimen geometry. Consequently, the associated average shear strain at the crack tip does not represent a true material property. In concluding this section, it is noted that in contrast to the CSIC, the analysis for the TSIC configuration shows that σ_{yy} changed from *tension* to *compression* as the distance from the crack tip is increased. This finding is clearly consistent with the lack of microdebonds in the TSIC tests.

4.3. Crack kinking and voiding

Crack kinking in linearly-elastic bi-materials is a well-known phenomena. The kink angle is generally taken to follow the principal tensile stress trajectory or the plane of zero shear. The prospect that this is also the case for the present large-strain problem (e.g. Fig 2(b,c)) is now examined. Figure 8(b) shows contours of maximum principal stress, $(\sigma_p)_{\max}$, at a given instance during crack propagation ($\bar{\gamma}_t = 0.12$) for case study no. 3. As shown, the principle stress is tensile, heavily concentrating at the crack tip. The variation of this stress with load is given in Fig. 13. As shown, $(\sigma_p)_{\max}$ gradually increases with increasing load, i.e. from zero at infinitesimally small strain to over 150% of the yield stress at the onset of crack propagation. Thereafter, $(\sigma_p)_{\max}$ remains essentially constant. The trajectory at which this stress is maximized is obtained by drawing a line from the crack tip such that it crosses each contour at a right angle. The resulting dashed curve [Fig. 8(b)] resembles an “S” shape which is quite similar to the crack kinking path depicted in Fig. 2(c), photo no. II. The kink angle, α , is taken as the initial angle of this trajectory with respect to the interface. As demonstrated in Fig. 11, this angle is found by drawing a straight line from the crack tip such that it intersects the arrows of the principal stresses at a right angle in the crack tip vicinity. The variations of the so evaluated kink angle with $\bar{\gamma}_t$ for case study no. 3 is given in Fig. 12 (solid curve). In the linearly elastic range ($\bar{\gamma}_t \ll 1$), α seems to approach $70 \sim 80^\circ$, which is consistent with results given by He and Hutchinson (1989) for an elastic medium on top of a nearly rigid substrate. The predicted kink angle decreases with increasing $\bar{\gamma}_t$, however, approaching $55\text{--}60^\circ$ at the onset of crack propagation ($\bar{\gamma}_t = 0.12$). Thereafter, α remains nearly constant. The conditions for crack kinking associated with the tests in Fig. 2 (b) and (c), Frame I of Fig. 2 (c), are $\alpha = 46^\circ$, $\bar{\gamma}_t = 0.11$ and $\alpha = 50^\circ$, $\bar{\gamma}_t = 0.62$,

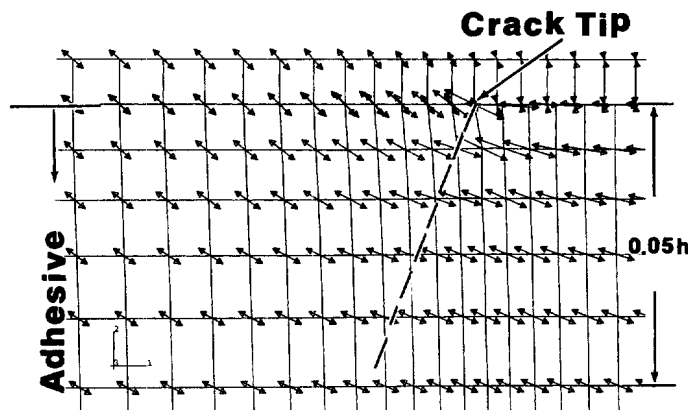


Fig. 11. A finite element plot showing the direction of the maximum principal tensile stress at the crack tip region for a rigid-substrate, TSIC model with $\bar{\gamma}_t = 0.01$. The kink angle is defined by the dashed line emanating from the crack tip which crosses the stress lines at a right angle.

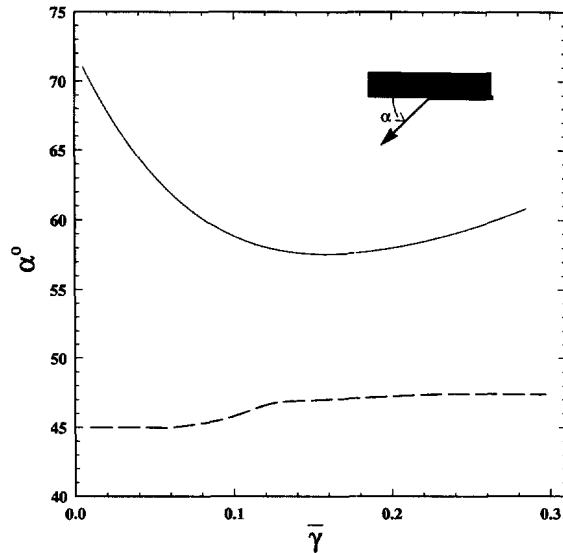


Fig. 12. Finite element predictions of the variations of the direction of the maximum principle tensile stress trajectory at the crack tip (solid line), α , and the plane of principal tensile stress corresponding to several bond thicknesses ahead of the crack tip (dashed line). Data pertain to case study no. 3.

respectively. These values are within 20% of the theoretical prediction given in Fig. 12. Also given in Fig. 12 (dashed line) is the orientation of the plane of maximum principal tensile stress pertaining to several bond thicknesses *ahead* of the crack tip. As shown, this angle (i.e. 45–47°) is quite insensitive to the deformation level.

While $(\sigma_p)_{\max}$ affects crack kinking, the mean stress, $\sigma_m (= (\sigma_1 + \sigma_2 + \sigma_3)/3)$ plays an important role in the formation and growth of voids or cavities, both for particulate metals [e.g. Mackenzie *et al.* (1977)] and rubber toughened epoxies [e.g. Huang *et al.* 1993]]. For the present macroscopically homogeneous adhesive, such damage is a consequence of the very large deformations which occurs in the bond. Figure 8(c) shows σ_m contours for a given load while Fig. 13 details the continuous variation of σ_m at the immediate vicinity of the crack tip during the fracture process for case study no. 3. As shown, the mean stress is tensile, and it is continuously increasing up to the onset of crack propagation. As for $(\sigma_p)_{\max}$ and α , σ_m remains essentially constant during the crack propagation. Noting that for the CSIC cases (i.e. case studies nos 1 and 2) the mean stress is compressive, and that no voids

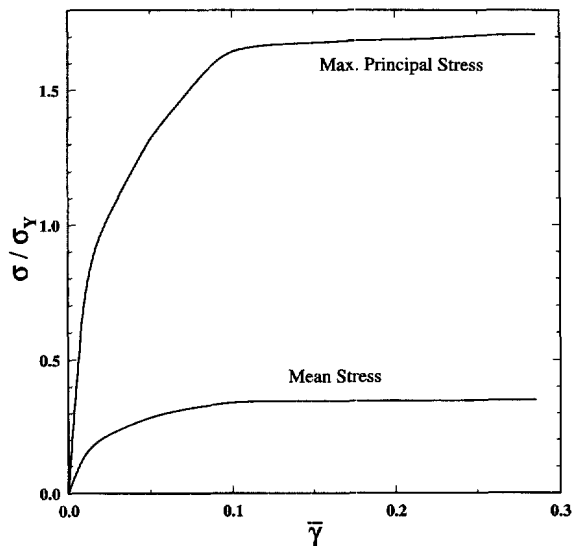


Fig. 13. Finite element prediction of the variation of the mean stress and the maximum principal stress at the crack tip with $\bar{\gamma}$ for case study no. 3.

were observed for these tests, it seems clear that the voids exhibited in Fig. 2(d) are a direct consequence of the development of σ_m at the crack tip with load.

The fact that the load necessary to initiate a kink or a void depends on the bond thickness (Fig. 3) is intriguing given that on a normalized length scale basis the elastoplastic fields for the rigid-substrates models are independent of h . To explain this dependence one apparently must resort to damage mechanics considerations. It can be argued that the development of inherent flaws into a kink or a void becomes less possible as the bond thickness and, therefore, the size of the stress concentration region from which such damage may form, is decreased. Assuming, for example, the dimension of this region to be one hundredth of the bond thickness, one has for the 420 μm and the 135 μm thick bonds in Fig 2(b,c) damage nucleation sizes of 4.2 and 1.35 μm , respectively. The latter dimension may approach the order of magnitude of inherent flaws, which makes the nucleation of a kink or a void less possible.

5. SUMMARY AND CONCLUSIONS

A large-strain, rate-dependent finite element analysis is carried out to help elucidate a crack propagation criterion for adhesive bonds undergoing very large shear deformations. Comparison of the analytical predictions with available test results shows that both the onset of crack growth and the stable interfacial crack propagation that follows are generally reasonably well-governed by the magnitude of the local engineering shear strain at a certain distance straight ahead of the crack tip. Over the range of parameters tested, this criterion is found to be insensitive to the specimen geometry, bond thickness and direction of applied shear. The departure between the analysis and the experiments may be attributed to various factors including the great sensitivity of the results to the input parameters and inadequacy of the material flow model used. More careful experimentation and analytical modeling is needed to more firmly establish the validity of the proposed fracture criterion.

The analysis provides semi-quantitative explanations for other experimentally observed failure modes. The onset of a microdebond ahead of the crack tip, in the case of a compression side interface crack, appears to be controlled by the bond-normal tensile stress. Once formed, this damage rapidly spreads in both directions under the action of the background shear stress causing catastrophic failure. For a given $\bar{\gamma}_c$, this bond-normal stress increases with h , which explains why the ultimate load of the joint, γ_1^d , decreases with increasing bond thickness. The development of a large void at the crack tip is attributed to tensile hydrostatic stresses. This damage causes a blunting of the crack tip, with temporarily precludes further crack growth. Finally, the kinking of a crack from the tension to the compression side interface appears to be governed by the maximum principal tensile stress at the crack tip. Unlike in LEFM, the kinking trajectory is found to be greatly affected by the magnitude of the background strain in the bond. All of these failure mechanisms occur under very large strains, which is a consequence of the ability of very thin polymeric adhesives to locally sustain very large deformation.

REFERENCES

- ABAQUS version 5.3 (1994) Hibbit, Karlsson and Sorensen, Providence, RI.
- Broeck, D. (1986) *Elementary Engineering Fracture and Mechanics*. Martinus Nijhoff, The Netherlands.
- Chai, H. (1993) Observation of deformation and damage at the tip of cracks in adhesive bonds loaded in shear and assessment of a criterion for fracture. *International Journal of Fracture*, **60**, 311–263.
- Chai, H. and Chiang, M. Y. M. (1996) A crack propagation criterion based on local shear strain in adhesive bonds subjected to shear. *Journal of the Mechanics and Physics of Solids*, **44**, 1669–1689.
- He, M. Y. and Hutchinson, J. W. (1989) Kinking of a crack out of an interface. *Journal of Applied Mechanics*, **56**, 270–278.
- Huang, Y., Hunston, D. L., Kinloch, A. J. and Riew, C. K. (1993) Mechanics of Toughening Thermoset Resins. In *Toughened Plastics*, Vol. I, ed. C. K. Riew and A. J. Kinloch, pp. 1–35. American Chemical Society, Washington, D.C.
- Liechti, K. L. and Knauss, W. G. (1982) Crack propagation at material interfaces: II experiments on mode interaction. *Experimental Mechanics*, 383–391.
- Mackenzie, A. C., Hancock, J. W. and Brown, D. K. (1977) On the influence of stress on ductile failure and initiation in high strength steel. *Elementary Engineering and Fracture Mechanics*, **9**, 167–188.

- McClintock, F. A. (1958) Ductile-fracture-instability in shear. *Journal of Applied Mechanics*, 582–588.
- Rouselier, G. (1979) Numerical treatment of crack growth problems. In *Advances in Elastoplastic Fracture Mechanics*, pp. 165–189. Applied Science Publishers, London.
- Wells, A. A. (1963) Application of fracture mechanics at and beyond general yielding. *British Welding Journal*, 563–570.
- Williams, J. G. (1984) *Fracture Mechanics of Polymers*. Wiley, New York.